p–Ω^- and p–Ξ^- Interaction with Two-Particle Correlation Femtoscopy at LHCb

Summer student report

Nicolas Himbert

CERN, Heidelberg University (DE)

Under the supervision of

Prof. Mikhail Mikhasenko

and

Dr. Thomas Pöschl

September 13, 2024

Abstract

This work presents the first measurement of the correlation function of $p - \Omega^-$ and $p - \Xi^-$ at the LHCb experiment using the full Run2 dataset and 2018 data respectively. An attractive interaction of the proton and the Hyperons was found which hints to a virtual state between the two particles. The measurement confirms the previous measurement of the ALICE collaboration. This work has a first look at the fresh Run3 data for dedicated femtoscopy lines and confirms that the HLT2 lines are producing reasonable mass peaks and estimates roughly the number of expected signal yields for the data taken to this date.

Contents

1 Introduction

This section gives a brief overview of the motivation and theory behind the measurement of correlation functions in the frame of femtoscopy.

1.1 Motivation

To study the Hyperon-Nucleon (YN) interactions there are several motivations. One of the main interests in study these systems originates from the astrophysical community. When one looks at neutron stars, which are remnants of massive stars of Type-II, Ib or Ic supernovae. With a mass of around 1-2 $M_{\odot}$ and a radius between 10-12 km they are one of the densest objects in the universe consisting of neutron rich matter which is β -stable matter. This refers to the equilibrium of the weak interaction. In the dense core of the neutrons stars there can appear additional degrees of freedom which can lead to the production of hyperons. In contrary to the conditions on earth where these baryons are short lived particles they can be formed under these conditions by leptonic decays in the central core at a density of $2 - 3\rho_0$. The presence of a certain amount of hyperons makes the interaction between hyperons and hyperons (YY) and hyperons and nucleons (YN) relevant. One of the main goals of the analysis of correlation functions (Analysis tool to study these systems) is to quantify these interactions.

For the astronomical understanding of the neutron stars it is crucial to understand the Equation of state (EoS). The EoS relates the pressure P, density ρ and temperature T. For cold neutron stars the temperature effects are negligible so the EoS can be simplified to:

$$P = P(\rho) \tag{1}$$

When the YN interaction is attractive the concentration of hyperons gets larger and the production of the hyperons starts earlier. This will relief the Fermi pressure and lead to a stronger softening of the EoS and final results in the reduction of the maximum mass. This means that the presence of hyperons will result in smaller masses of the neutron stars. When one calculates the EoS for neutron stars like in Figure 1(b) with (red) and without (black) hyperons one can see that the maximal mass of the neutron stars decreases. The interesting observation is that there are some neutron stars observed that have larger masses than the theoretical calculated ones. This is the so called Hyperon puzzle. There are three possible solutions to the puzzle: (i) A repulsive YY interaction could stiffen the EoS and increase the maximal mass of the neutron stars, (ii) A repulsive hyperonic

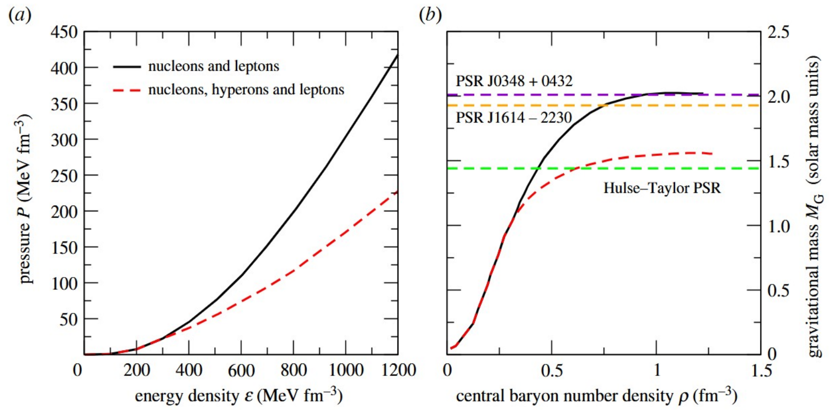

Figure 1: Impact of the inclusion of hyperons in the EoS of neutron stars in (a) the pressure as a function of the energy density and (b) the gravitational mass against ρ. For nucleons and leptons (black) and nucleons, hyperons and leptons (red). Vertical lines in (b) indicate astronomical measurements of selected neutron stars [1].

three-body force or (iii) the possibility of a phase transition to deconfined quark matter at densities below the hyperon threshold.

This was only one of the motivations to study these systems. Another one is the interest from the effective field theorist when working with lattice calculations since they need to fix the low energy constants and since the correlation functions can probe precisely the low momentum YN interactions [2].

The Hadron to Atomic Level QCD (HAL QCD) collaboration predicts a $p{-}\Omega^-$ (uudsss) bound state with a binding energy of 2.46 MeV which results in a specific shape of the attractive correlation function. With a complex shape that can be modelled but will result in an attractive correlation near the threshold [3].

1.2 Previously measurement

This paper will concentrate on the measurement of the YN interaction in $p{-}\Xi^-$ and $p{-}\Omega^-$ at the LHCb experiment. There is a previously measurement by the ALICE collaboration in 2020 which found an attractive interaction in these systems. The results are shown in Figure 2. One can see that $C(k^*)$ approaches 1 for large k^* and for both systems there is an enhancement in the interaction near the threshold. For $p-\Xi^-$ the data points are compatible with the HAL QCD calculations when adding the coulomb term. For the $p{-}\Omega^-$ this is only partially true for the elastic approximation but this approximation fails in the range $k^* \in [100; 250]$ MeV, where the theoretical calculation predicts a small depletion in

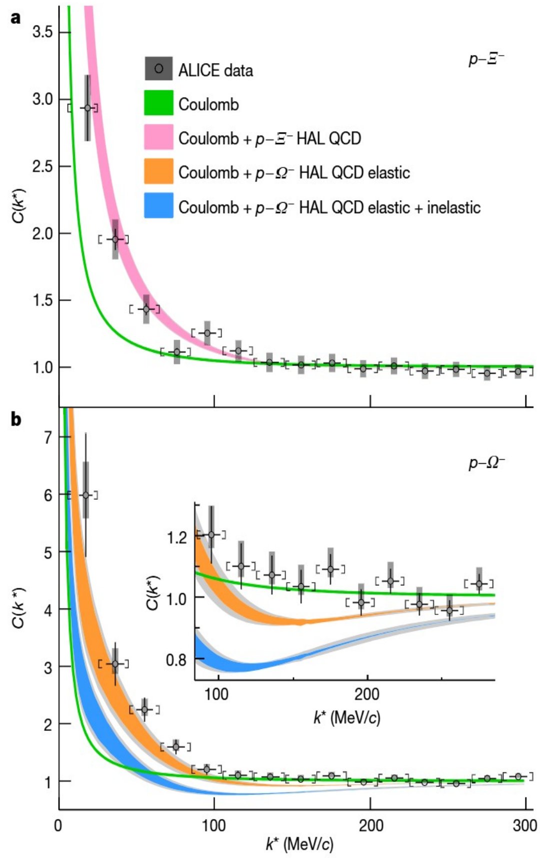

Figure 2: Correlation function $C(k^*)$ as a function of 20 MeV bin of k^*. In (a) for $p{-}\Xi^-$ and in (b) for $p-\Omega^-$. In the grey boxes the systematic uncertainty and as error bars the total error. Overlaid with different theoretical calculations from the HAL QCD collaboration [4].

the correlation function (which would describe a bound state) [4].

1.3 Correlation function in femtoscopy

The term femtoscopy refers to the source-size in heavy-ion collisions, which is approximately a few fm. This source size refers to a spherical approximation where after a heavy-ion or proton-proton collision the hadronisation takes place and as a result final state particles are emitted. For the study of correlation functions only the final state interaction between two or more particles is relevant. Nevertheless one has to take into account that possible resonances can occur inside of the emission source and need to be modelled in the theoretical predictions. The physical observable that can be measured with the data from the experiment is the so called correlation function $C(k^*)$ which is described in the

2-particle rest frame. There the relative momenta between the two particles in the rest frame is given by:

$$k^* = \frac{1}{2} \mid \vec{p}_1^* - \vec{p}_2^* \mid = \frac{\sqrt{\lambda(m_{12}^2, m_1^2, m_2^2)}}{2m_{12}}, \tag{2}$$

where λ is the fully symmetric Källén function:

$$\lambda(a,b,c) = a^2 + b^2 + c^2 - 2ab - 2bc - 2ac, \tag{3}$$

m_{12} the invariant mass of the two particles and m_1, m_2 are the separate masses of the two particles.

And from there the correlation function $C(k^*)$ is given as:

$$C(k^*) = \xi(k^*) * \frac{N_{same}(k^*)}{N_{mixed}(k^*)}, \tag{4}$$

where $N_{same}(k^*)$ gives the number of same events for a given k^*. The term same event refers to the fact that the two particles originate from the same event and a correlation is present between them. In the mixed events, $N_{mixed}(k^*)$, the two particles are not from the same event and no interaction between them is present. The mixed events model the underlying phase space of the two particle interaction. The uncorrelated pairs can be created by mixing the events of one particle with respect to the other and recalculate the number of events as a function of k^*. The normalisation factor ξ is used to normalise the correlation function to 1 at $k^* > 300\text{MeV}$, since it is expected that there is no signal present. The boundary for the normalisation is not a fixed value and can be varied in a reasonable range. The normalisation takes also care of some detector effects.
In general some systematic uncertainties are cancelled out in the correlation function, since in the mixed and same events the same data is used and after combining differently they are divided by each other. For example selection efficiencies cancel out.

$$C(k^*) = \begin{cases} > 1 & \rightarrow \quad \text{attractive} \\ < 1 & \rightarrow \quad \text{repulsive} \end{cases}. \tag{5}$$

As a quantitative interpretation of the correlation function it is sufficient to classify the correlation function into two parts. When $C(k^*)$ is larger than 1 the interaction between the two particles is attractive and the k^* region where the correlation is attractive is more probable. When the correlation function is enhanced near the threshold at $k^* = 0$ a virtual

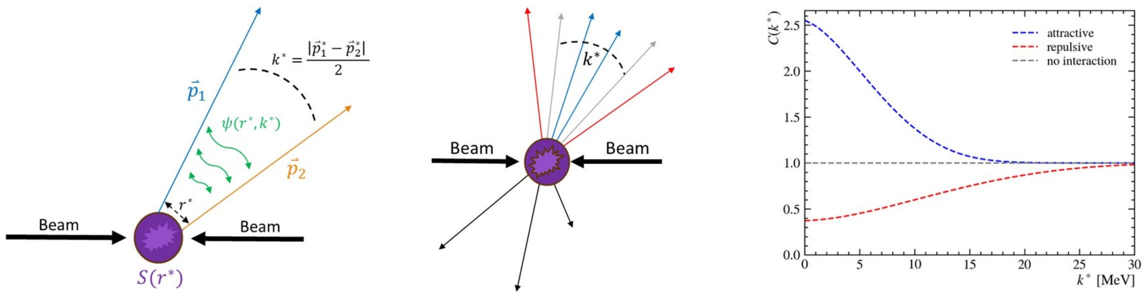

Figure 3: Schematic representation of the correlation function. Representation of the emission source and wave function in a collision system at the LHC (left). Representation of an attractive interaction (blue) where the probability of smaller k* is larger and the correlation function is > 1 (right) and for a repulsive interaction (red) where a depletion near the threshold is visible.

or bound state between the two particles can be formed. In contrary when $C(k^*)$ is smaller than 1 the interaction is repulsive.
The correlation function can be viewed from a more theoretical point of view where it can be expressed as:

$$C(k^*) = \int d^3\vec{r}^* \mid \psi(k^*, \vec{r}^*) \mid^2 S(\vec{r}^*). \tag{6}$$

Here the $S(\vec{r}^*)$ is the emission source function with the radius of the source given by $\vec{r}^*$. The source function can be approximated as a Gaussian function, but does not need to be spherical symmetric and can have a different parametrisation. This is a field of study where more techniques need to be explored to achieve this. The wave function that describes the interaction between the two particles is given by $\psi(k^*, \vec{r}^*)$. It can be calculated by using the stationary solutions of the Schrödinger equation. To calculate the theoretical values of the correlation function one can use the CATS [5] tool [6].

1.4 Relation between k^* and the invariant mass

The relative momentum between the two particles k^* is related to the invariant mass with the formula given in Equation 7.

$$m_{12}(k^*) = \sqrt{m_1^2 + m_1^2 + 2k^* + 2\sqrt{((k^*)^2 + m_1^2)((k^*)^2 + m_2^2)}}. \tag{7}$$

So for a given k^* only the rest masses of the two involved particles are need. For the $p-\Omega^-$ and $p-\Xi^-$ system one can calculate the difference in the invariant mass range in the range of $k^* \in [0; 300]$MeV:

$$m(p) = 938MeV$$
$$m(\Omega^-) = 1672.45MeV$$
$$m(\Xi^-) = 1321.7MeV$$

$$\Omega^- : m_{12}(300MeV) - m_{12}(0MeV) = (2684 - 2610.45)MeV = 73.55MeV \tag{8}$$

$$\Xi^- : m_{12}(300MeV) - m_{12}(0MeV) = (2340.1 - 2259.7)MeV = 80.4MeV \tag{9}$$

The range in k^* corresponds to an invariant mass range of around 80 MeV for $p - \Omega^-$ and $p - \Xi^-$.

1.5 Theoretical model of the correlation function

The correlation function can be modelled using the CATS framework or one can use a new formalism which is described in [7]. There the authors are able factor out the scattering amplitude from the integrals. In this section the convention k=k^* is used to make the formulas more readable.

The formula from the paper can be written in a way that k^* and all masses are given in Mev (and before the calculation converted to fm^{-1}.
The main integral is given as:

$$\begin{gathered}1 + 4 * \pi * \Theta(q_{max} - k) * \int_0^\infty dr * r^2 * S(r, R) * (\mid j_0(kr) + T_1(a, k, E) \\ * G_1(r, E, q_{max}, \eta) \mid^2 + \mid T_1(a, k, E) * G_1(r, E, q_{max}, \eta) \mid^2 - j_0(kr)^2).\end{gathered} \tag{10}$$

In this function the emission source S(r,R) is given by:

$$S(r, R) = \frac{1}{(\sqrt{4\pi}R)^3} * e^{-\frac{r^2}{4R^2}}, \tag{11}$$

where R is the emission source radius. A Breit-Wigner like function with an energy prefactor:

$$T_1(a, k, E) = -8\pi E * \frac{1}{-\frac{1}{a} - ik}. \tag{12}$$

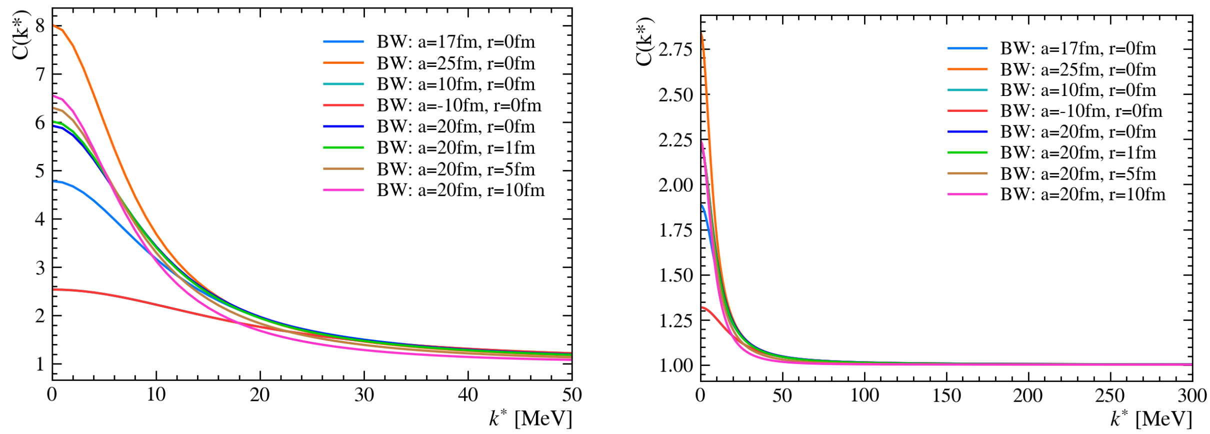

Figure 4: Normalised Breit-Wigner approaches for the correlation function near the threshold for different relation between the scattering length a in fm and source radius r in fm. For $k^* \in [0;50]$MeV (left) and $k^* \in [0;300]$MeV (right).

is needed. Additional the zeroth spherical Bessel function is given by:

$$j_0(kr) = \frac{\sin(kr)}{kr}. \tag{13}$$

As a last equation:

$$\begin{aligned} G_1(r, E, q_{max}, \eta) = \int_0^{q_{max}} dq * \frac{4\pi}{(2\pi)^3} * q^2 * \frac{j_0(qr)}{E^2 - (\sqrt{m_1^2+q^2} + \sqrt{m_2^2+q^2} + q^2)^2 + i\eta} \\ * \frac{\sqrt{m_1^2+q^2} + \sqrt{m_2^2+q^2} + q^2}{2 * \sqrt{m_1^2+q^2} * \sqrt{m_2^2+q^2}}. \end{aligned} \tag{14}$$

To this equation some explanation is needed. The quantity q_{max} determines the range of the interaction in momentum space and is approximated with 420 MeV. The width of the particle state is given by $\eta = 1e^{-3}$. The masses of the two particles are taken from section 1.4.

The energy E is given by:

$$E = \sqrt{m_1^2 + k^2} + \sqrt{m_2^2 + k^2}. \tag{15}$$

Another approach is plotting a simple Breit-Wigner distribution with a constant background:

$$C(k) = \mid T(a, r, k) \mid^2 + b, \tag{16}$$

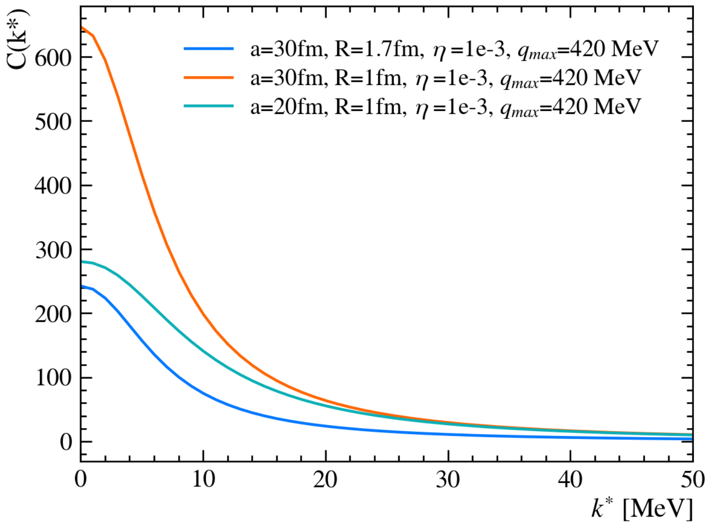

Figure 5: Correlation functions modelled with the approach given in [7] for different scattering lengths and emission source radii. The functions are not normalised to the plotting interval.

with

$$T(a, r, k) = \frac{1}{\frac{1}{a} + \frac{rk^2}{2} - ik}, \tag{17}$$

where i is the imaginary unit and a is the scattering length in MeV and b is the constant background term which is set to b=1 for the normalisation. If a > 0 and r $= 0$ the shape describes a bound state whereas for a < 0 (r $= 0$) a virtual state is modelled. To model a resonance r < 0 and a > 0 is needed.

For the approach given in formulae 16 and 17 for different source radii and scattering length the correlation functions are plotted in Figure 4. The function is normalised to the plotting range of k^*, this is crucial since only this way the shapes can be compared properly.In the plots it can be seen that a higher scattering length results in a higher value of the correlation function at the threshold for a fixed r. For a fixed scattering length the variation of r results in a slightly change in the maximal value of the correlation function but also for higher higher r the shape gets squeezed in k^*. In general the shape is only present near the threshold, which is expected. In red a example for a virtual state is plotted and overlaps with the bound state with the negative scattering length. So the BW function is not able to differentiate between a virtual and a bound state when the absolute value is plotted. A further conclusion from these plots is that it is necessary that the binning

needs to be small enough since it is not sufficient to discriminate the different curves for a wide binning. The binning chosen by ALICE will not resolve all of the r-dependencies shown in the plots. The binning can only made smaller if the statistics increases.
The plot for different assumptions for the more complex from formula 14 can be seen in Figure 5. Here the functions are not normalised due to the long computation time for the sequential integrals in the calculation. But the same trend as before can be seen, so that for larger a and same R the maximal value near the threshold increases and for larger R at same a the function gets squeezed to the threshold.

2 Analysis

This section is split into an introduction to the analysis strategy and the data sets used in this analysis, the online and offline selection criteria, the mixing algorithm and the results. In the following the convention $p - \Omega^- \equiv p - \Omega^- \oplus \overline{p} - \Omega^+$ is used.

2.1 Analysis strategy

The analysis is based on the selection of the decays with dedicated stripping lines to build first the hyperon decays and than including the proton, which is needed for the correlation, in the DaVinci framework. After the building of the decay the background for the hyperons is reduced and the proton is selected such that there is as less as possible contamination from other particles left. This is crucial since one is interested in the correlation of the specified particles and since it is an precision experiment this plays a crucial role. After the selection based on rectangular cuts a event mixing is applied to calculate the correlation function $C(k^*)$.

2.2 Datasets/Stripping selection

The two YN interactions which are analysed are the $p - \Omega^-$ and $p - \Xi^-$.

For the $p - \Omega^-$ the full Run2 dataset is used and is reconstructed as $\Omega^- \to (\Lambda^0 \to \pi^- p)K^-$ in the "Omegaminus2LambdaK" stripping line. Since the Ω^- has a mean flight distance (FD) of around 28cm it can decay inside or outside of the Velo and the K^- can be reconstructed as a long track or downstream track. This results in different cuts in the stripping line which can be seen in Table 1. This is the reason this dataset is divided into two subsets for the different track reconstructions and are denoted K_{long} and K_{down} for the long track and downstream track respectively. The Λ^0 decays after an additional mean FD of 1.5m into two downstream tracks of a proton and pion. Since the stripping line does not distinguishes in the final ROOT file between the two lines a cut on the z-position of the own primary vertex (PV) of the Kaon is applied. For values <650mm the event is assumed to follow a long track and > 650mm for a downstream track. This a valid approximation since the Velo has a length of 750mm and for a long track a sufficient amount of hits in the Velo modules are necessary.

For the $p - \Xi^-$ only the 2018 data with both magnet configurations is used. The Ξ^- is reconstructed via the "Ximinus2LambdaPi" stripping line where the decay $\Xi^- \to (\Lambda^0 \to \pi^- p)\pi^-_{bach}$ is used. The notation π^-_{bach} is used to differentiate the two pions in the decay.

Table 1: Stripping line cuts Ω^- for the different stripping selections depending on the track of the Kaon.

Particle	**Variable**	K^-_{long}	K^-_{down}
Ω^-	mass constrain	< 25 MeV	
	BPV_τ	> 0.005 ns	
	BPVVDZ	>0	
	Δz_{vertex}	> 5	
	$v_{\chi^2/ndof}$	< 5	
Λ^0	mass constrain	< 5.7 MeV	
	v_z	$\in [400; 2275]$mm	
	$v_{\chi^2/ndof}$	< 5	
π^-	p_T	> 100 MeV	
K^+	p_T	> 100 MeV	
	PID_K	$>$ -5	
	$track_{\chi^2/ndof}$	< 3	
	$ProbNNk$	> 0.2	
	$BPV - IP_{\chi^2}$	> 100	
	$track_{GhostProb}$	< 0.25	—

Since the Ξ^- has a mean FD of 1m the π^-_{bach} is only reconstructed as a downstream track. The applied cuts by the stripping line can be seen in Table 2.

To perform the correlation function the hyperon decays need to be combined with a proton. This is done with the CombineSelection-Tool in DaVinci. The proton is reconstructed using the "StdAllLooseProtons" stripping line. This line provides protons with only applied loose cuts. This is chosen to be able to study and tune the offline selection cuts such that the contamination of other particles is minimised. In the following this proton is also called p_{bach} to distinguish it from the proton originating from the Λ^0. The decay topology of the two combined decays can be seen in Figure 6.
A summary of the datasets and the yields of the selected data after the stripping lines can be found in Table 3.

2.3 Offline selection

To achieve the precision needed to perform a reliable result of the correlation function a dataset with a high purity is needed. This is only be achieved by applying offline selection cuts to the datasets to reduce the background and not loosing too much signal yield. There are two major selection techniques: one based on a boosted decision tree (BDT) or neural net (NN) to separate signal from background using a signal proxy such as Monte

Table 2: Stripping line cuts Ξ^-.

Particle	Variable	Cut
Ξ^-	mass constrain	< 25 MeV
	BPV_τ	> 0.005 ns
	BPVVDZ	>0
	Δz_{vertex}	> 5
	$v_{\chi^2/ndof}$	< 5
Λ^0	mass constrain	< 5.7 MeV
	v_z	$\in [400; 2275]$mm
	$v_{\chi^2/ndof}$	< 5
π^-_{bach}	p_T	> 100 MeV
	PID_K	< 5
	$track_{\chi^2/ndof}$	< 3
	$BPV - IP_{\chi^2}$	> 100
p^-	p_T	> 500 MeV
	$ProbNNp$	> 0.05
π^+	p_T	> 100 MeV

Table 3: Different datasets and there yields after the stripping line.

Correlation	**Year**	K^- **stripping**	**Magnet**	**Yield (after stripping)** $[10^6]$
$p - \Xi^-$	2018	—	Both	69.69
$p - \Omega^-$	Total Run2	Long/Down	Both	63.3/7.72

Carlo (MC) simulations or applying rectangular cuts to the dataset. The later is not fully optimised since the correlation between the different variables is not taken into account. In this section the rectangular cuts are used since there were no MC simulations available at the time of the analysis.
The offline selection is split in two parts. The first parts deals with the selection of the hyperons while the second subsection focuses on the selection of a clean proton.

2.3.1 Hyperon selection

A measure that is used to quantify the selection is the purity:

$$\text{purity} = \frac{S}{S+B}, \tag{18}$$

where B is the background yield and S the signal yield extracted by a fit to the invariant mass spectrum of the hyperon. In this work a JohnsonSU function [8] is used for the signal

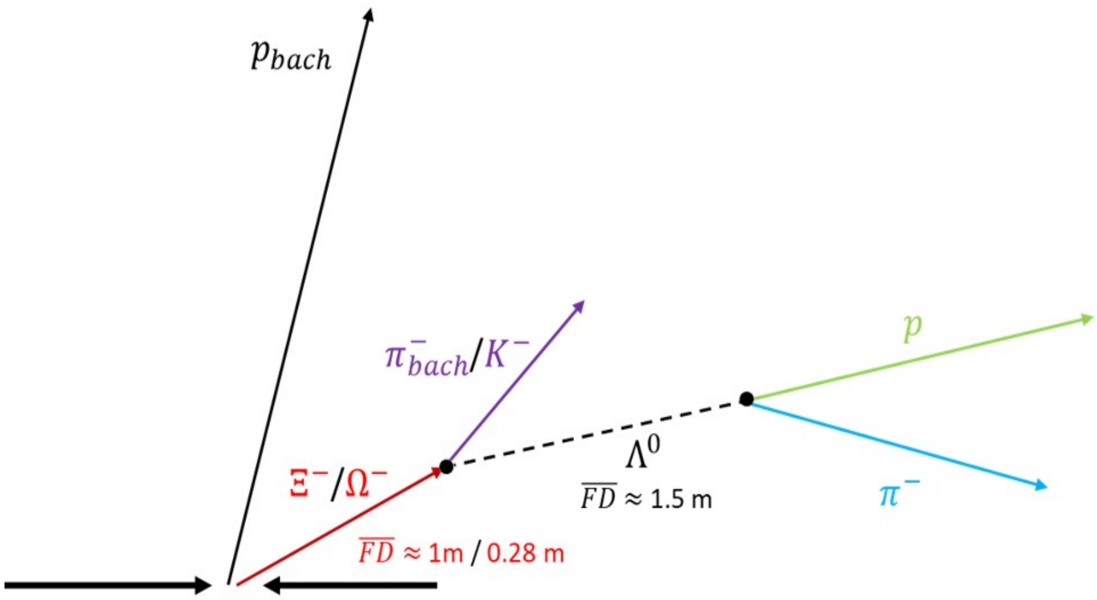

Figure 6: Schematic decay topology of the $p - \Omega^-$ and $p - \Xi^-$ decays.

fit and a second order polynomial for the background.

$$\text{JohnsonSU}(x) = \frac{\delta}{\lambda\sqrt{2\pi}} \frac{1}{\sqrt{1 + \left(\frac{x-\xi}{\lambda}\right)^2}} \exp\left(-\frac{1}{2}\left(\gamma + \delta \sinh^{-1}\left(\frac{x-\xi}{\lambda}\right)\right)^2\right). \tag{19}$$

Initially the Ξ^- has a purity of 70.95%, the Ω^-_{long} 50.5 % and the Ω^-_{down} one of 52.2 %. These values are evaluated after the stripping line cuts.
For the optimisation of the selection cuts the figure of Merit (FoM) is plotted against the cut of a variable. As a FoM in the case of this work the significance (20) is used. There a scan for different cut values of a specific variable is performed and for each cut the signal and background yields are extracted by a fit. Here a JohnsonSU function for the signal and a linear background is used. This is in contrary to the above described fit function to determine the purity, but is necessary since the cut on the variables can result in a strongly fluctuating background when approaching hard cuts. To deal with this problem the linear background provides the most robust solution, since it is the most simple function. From the extracted fit the significance of the cut is calculated using:

$$\text{significance} = \frac{S}{\sqrt{S+B}}. \tag{20}$$

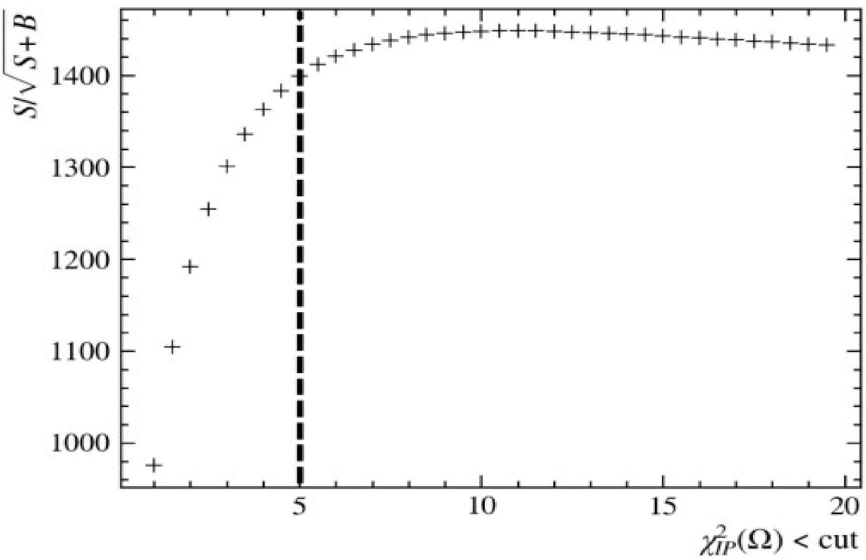

Figure 7: The significance is plotted against the cut on the χ^2_{IP} of the Ω^-_{long}.

The optimised cut value is chosen by hand on the FoM and aims for the highest significance. An example for such a FoM can bee seen in Figure 7.

The procedure described above is repeated for various kinematic and particle identification (PID) variables. More variables are tested before on only a few number of cuts to see the effect. This minimises the number of variables that are needed to be optimised and only use the variables that have the strongest influence on the background reduction. The variables like χ^2_{IP} are used to ensure that the hyperons originate from a primary vertex (PV) so that no resonances are taken into account which can influence the correlation function. Also variables of the ProbNNghost are used to reduce the ghost probability of the daughter tracks of the Λ^0. PID cuts are further applied to the charged children.
The procedure is performed on the three samples and a conclusion of all cuts can be found in Table 4 and Table 5.
For the Ω^-_{long} sample a purity of 92.24 % after the cuts is reached. To enhance that further a mass cut to the Ω^-_{long} is applied in the range of [1665;1680] MeV to enhance the purity to 95.78%. For the two other samples a high purity >99% is reported.

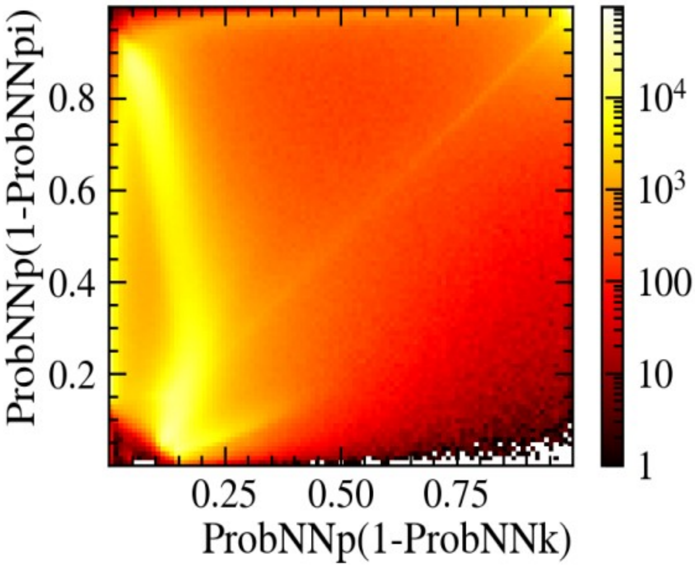

Figure 8: 2d plot of PID variables from a NN that takes RICH and track information into account, before any cuts on the proton are applied.

2.3.2 Proton selection

As described before the p_{bach} is selected with a loose stripping line so only loose cuts on the PID and the momentum are applied to the candidates. In Figure 8 one can see a two dimensional plot of ProbNNp(1-ProbNNpi) against ProbNNp(1-ProbNNk).

This plot is used since it shows on the top right a region where the protons are located and on the left side a band with various contamination's from other particles that were not classified by the neural net that produced the ProbNN variable. Since the LHCb detector uses Ring Imaging Cerenkov (RICH) detectors for the particle identification based on the Cerenkov angle of particles originating of the difference in the speed of light inside of a medium, the particles need to fulfil some momentum requirements so that the detector is able to separate the angles. In this case a momentum range of [12;100] GeV is required.

This is necessary since below 12 GeV the Kaons are not able to produce Cerenkov light and above 100 GeV the angle for Kaons and protons approaches each other so close that they are not distinguishable. See Figure 9. The lower boundary has a strong effect on the final correlation function, since for small relative momenta also small momenta from the proton are necessary. Further requirements are the flags that the particles is detected in the RICH, is no Muon and is above the proton threshold in the RICH. A further requirement is the constraint on the χ^2_{IP}, as for the hyperons. After these requirements one can now

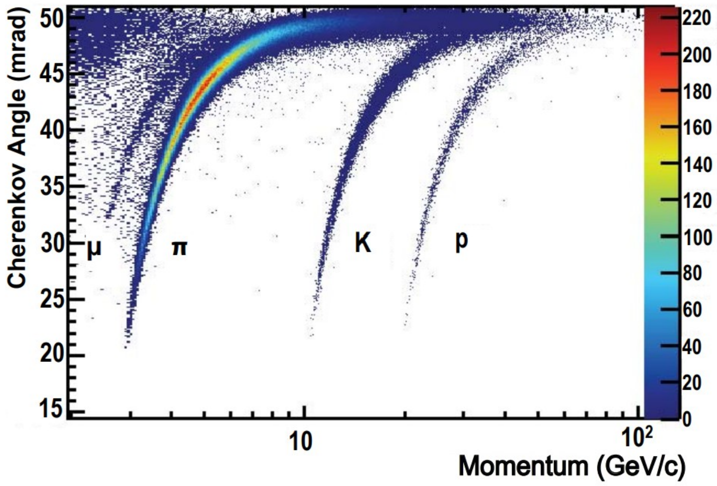

Figure 9: Cherenkov angle in mrad against the momentum of the particle in GeV for different charged particles in the RICH1 medium [9].

see in the 2d plot inf Figure 10 that now the protons can be clearly separated from Kaons and Pions.

To separate the charged hadrons in Run2 of the LHCb the delta-log-likelihood (DLL) is used since it performs better than the ProbNN variables. In this analysis the DLL_π for the proton was not available in the Ntuple and so not cut could be applied to the $DLL_{p\pi}$ variable and only on the DLL_{pk} variable. For new selection cut the author of this work would encourage the reader to use these variables instead of the one used here and follow the approach of [10]. For this work a cut on ProbNNp is avoided since it was observed that a direct cut on this variable can lead to a cut in the signal region and artificially tune the shape of the correlation function. This leads to the cut on the ProbNNpi<0.15 and to the cut of the $DLL_{pk} > 10$ adapted from [10]. To check for potentially clones and provide a cross check one can have a look at the angular distribution function between p_{bach} and the hyperon:

$$\theta = \cos^{-1}\left(\frac{\vec{A}\cdot\vec{B}}{\|\vec{A}\|\|\vec{B}\|}\right). \tag{21}$$

The distribution after all the selection cuts applied can be seen in Figure 11. Here no artificial peaks can be seen as it was the case prior with some contamination where a peak around 0.5 mrad was visible.

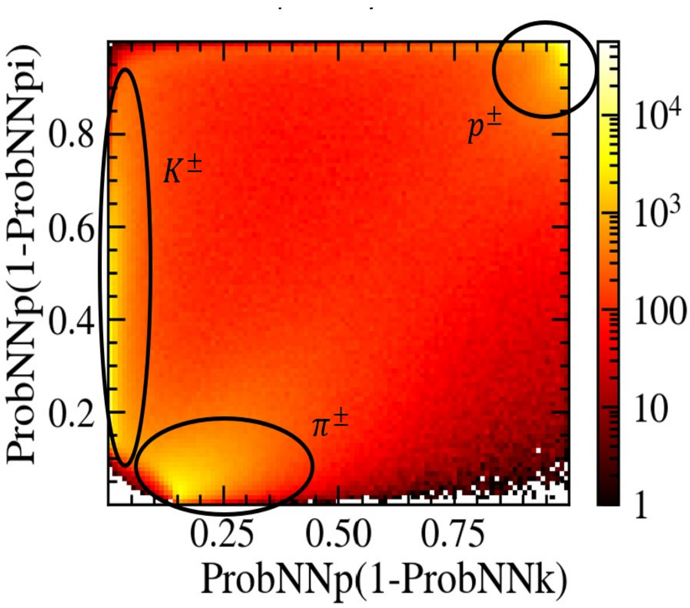

Figure 10: 2d plot of PID variables from a NN that takes RICH and track information into account. Offline cuts on the RICH requirements and kinematic cuts are applied.

2.3.3 Final fits after all selection cuts

The selection cuts for the p_{bach} and the hyperons are described above and are optimised. One can see the fits after the selection cuts of the two subsections above to the samples in Figure 12. All used cuts are shown in Table 4 and Table 5.

2.4 Mixing algorithm

As explained in the introduction chapter the key feature of the correlation function $C(k^*)$ is the calculation of N_{mixed}. This quantity is used to model the underlying phase space of the interaction. This can be calculated using uncorrelated pairs of protons and hyperons. Since N_{mixed} is a function of k^* it has to be calculated in the same bins as the N_{same} distribution so the two can be divided bin by bin to create the final correlation function. To understand the k^* distribution one can have a closer look at the definition:

$$k^* = \frac{\sqrt{\lambda(m_{12}^2, m_1^2, m_2^2)}}{2m_{12}}, \tag{22}$$

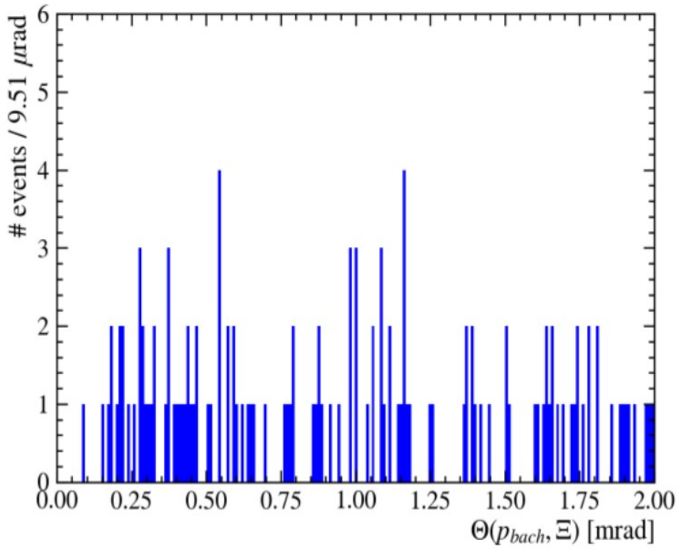

Figure 11: Angular distribution of p_{bach} and Ξ^- in mrad in a selected angle range where clones would be visible.

where λ is the fully symmetric Källén function:

$$\lambda(a, b, c) = a^2 + b^2 + c^2 - 2ab - 2bc - 2ac, \tag{23}$$

and m_{12} is the invariant mass of the two particles and m_1 and m_2 are the separate masses of the two particles. The invariant mass depends on the mass of the two particles and the 3-momenta. To create uncorrelated pairs of the two particles it is sufficient to change the 4-momenta of the one particle with respect to the other. This work uses the 4-momenta information of the proton. The array are shuffled with a given seed so that all the momenta and mass information of the same proton event are still combined. After the random shuffle the k^* distribution can be calculated as described above. But since the mixed event can be obtained in different ways one can increase the statistics by shifting after the first shuffling of the proton event and recalculate again the k^* distribution. This means one has now double the statics when adding the counts in each histogram bin. This procedure with the shifting can be repeated as much as the computation time allows. Another constrains for the shifting is that the one can only shift N-1 times till the same event in the mixed events occur, than one could in principle shuffle with another seed again. This leads in the end to a much higher statistics than in the same sample. In the scope of this work it is sufficient to shift on the order of 1000.

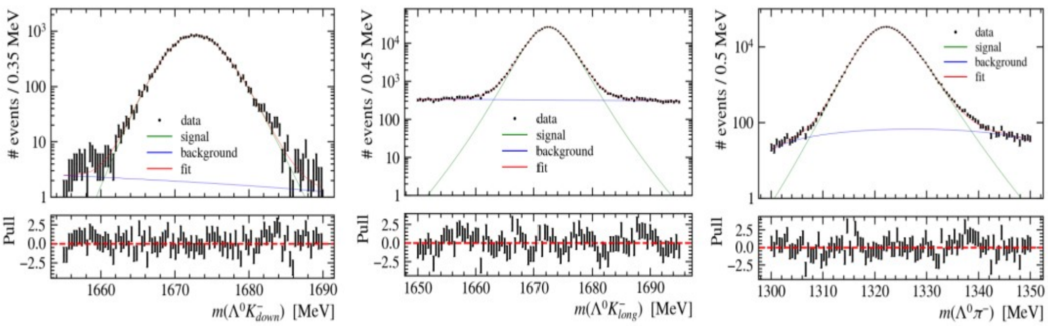

Figure 12: Fit to the invariant mass of the three hyperon sets. The fit (red) consist of a second order polynomial as a background (blue) and a JohnsonSU function for the signal (green). The y scale is plotted logarithmic to see the background shape more precise.

The lower bound for the number of shifting is the reduction of $\delta C(k^*)$ which is given as:

$$\frac{\delta C(k^*)}{C(k^*)} = \sqrt{\frac{1}{N_{same}(k^*)} + \frac{1}{N_{mixed}(k^*)}}. \tag{24}$$

This is calculated with Gaussian error propagation and assumes a error in each bin of k^* following a Poisson error of $\delta y = \sqrt{y}$. In the limit of $N_{mixed}(k^*) >> N_{same}(k^*)$ the error of the correlation function approaches:

$$\frac{\delta C(k^*)}{C(k^*)} \approx \sqrt{\frac{1}{N_{same}(k^*)}}, \tag{25}$$

and is independent of the mixing and only depends on the number of real signal events obtained by the dataset.

2.5 Results

To obtain the final $C(k^*)$ the simple step of dividing the two histograms obtained in the subsection above is missing. After that the distribution is normalised for convention to 1 in the range where the femtoscopy signal can be approximated to be absent. As a convention the region of $k^* > 300 MeV$ is used, but since in this region the correlation function is not really constant because detector acceptance effects play a role. That is the reason why a normalisation region of $k^* \in [240; 340]$MeV is chosen. The binning in k^* is set to 20 MeV and in the same bin boundaries as the ALICE measurement. In principle the bins can

Table 4: Summary of the selection cuts for $p - \Xi^-$.

Particle	Variable	Cut
Ξ^-	χ^2_{IP}	< 8
π^-_{bach}	ProbNNghost	< 0.94
	ProbNNpi	> 0.6
π^-	ProbNNghost	< 0.98
p	ProbNNp	> 0.6
p_{bach}	p	$\in [12; 100]$ GeV
	p_T	$\in [0.4; 4]$ GeV
	DLL_{pK}	> 10
	χ^2_{IP}	< 10
	ProbNNghost	< 0.15
	ProbNNpi	< 0.05
	hasRich	True
	isMuon	False
	RichAbovePrThres	True

be chosen arbitrary the problem for smaller bin widths is the lower statistics resulting in insignificant error bars.

2.5.1 Result for the $p - \Xi^-$ interaction

The result of $p - \Xi^-$ can be seen in Figure 13 for the zoom in the signal region and also for a larger region of k^*.

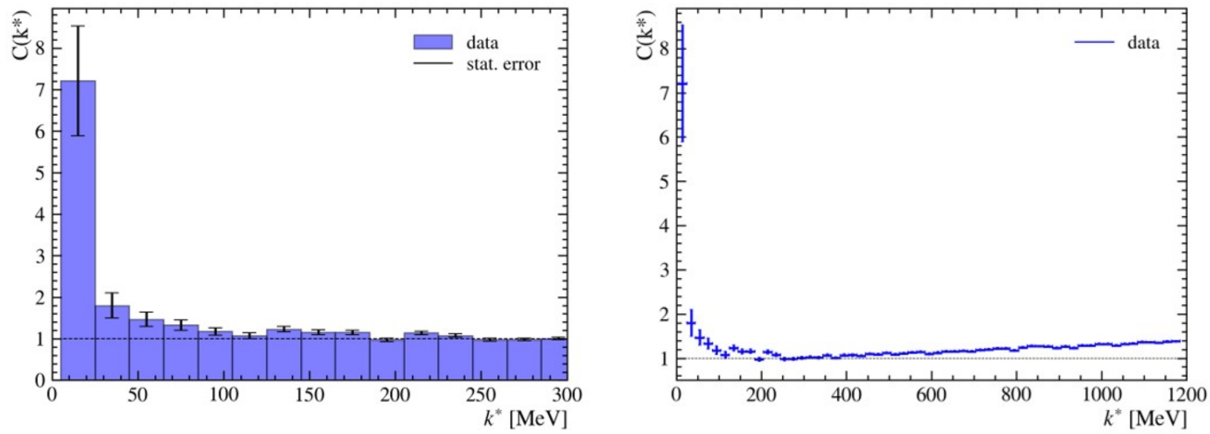

Figure 13: Correlation function of $p - \Xi^-$ for two different rage of k^*. On the left plot the range near the threshold $k^* \in [5; 300]$MeV and on the right plot for $k^* \in [5; 1205]$MeV.

One can see in the result that for the normalisation region the correlation function is

Table 5: Summary of the selection cuts for Ω^-_{long} and Ω^-_{down}.

Particle	**Variable**	$K^-_{\textbf{long}}$	$K^-_{\textbf{down}}$
Ω^-	χ^2_{IP}	< 5	< 8
	m	$\in [1665; 1680]$MeV	—
K^-	ProbNNk	> 0.3	> 0.6
π^-	ProbNNpi	> 0.5	
	ProbNNghost	< 0.96	< 0.97
p	ProbNNp	> 0.5	
p_{bach}	p	$\in [12; 100]$ GeV	
	p_T	$\in [0.4; 4]$ GeV	
	χ^2_{IP}	< 10	
	ProbNNghost	< 0.15	
	DLL_{pK}	> 10	
	ProbNNpi	< 0.05	
	hasRich	True	
	isMuon	False	
	RichAbovePrThres	True	

set to 1 when going to larger k^* the correlation function has a small attractive interaction, but as said above this is due to detector effect since at this high relative momenta there is no more interaction present between the two particles. In the left plot in Figure 13 the region near the threshold can be seen and it is a clear attractive interaction visible. The statistical error is only limited to the signal. This result confirms the measurement from the ALICE collaboration which can be seen in Figure 14.

In the comparison it can be seen that this work is on a good track to approach the results from the ALICE collaboration. Since only the statistical error in both cases are plotted an improvement of the statistics for LHCb is necessary to outperform. One of the main problem is probably the cut on the momentum acceptance to identify the proton. A possibility to deal with this was already mention above in the offline selection chapter. It could be possible to avoid the momentum cut when only using the DLL information. This is of course highly speculative but should be taken into account and the proton selection criteria should be revisit.

2.5.2 Result for the $p - \Omega^-$ interaction

The result for the correlation function in $p - \Omega^-$ are similar to the one for $p - \Xi^-$. A key difference is the splitting of the sample into the two sub samples from the stripping line.

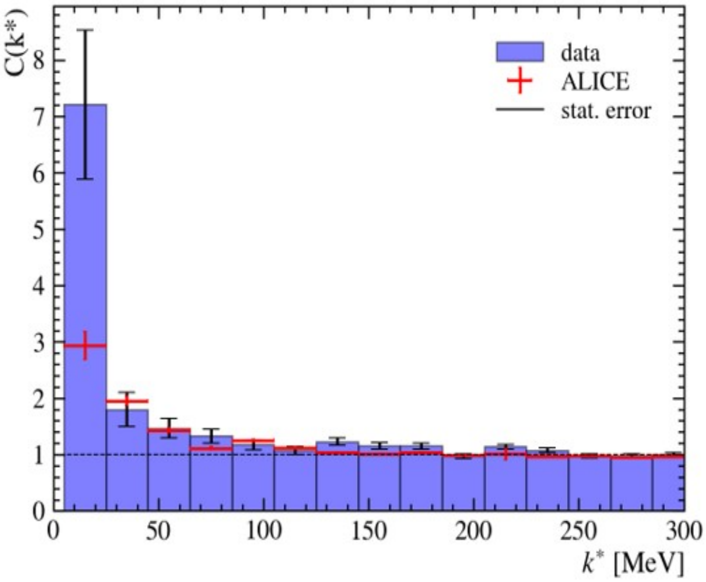

Figure 14: Comparison of the correlation function of $p - \Xi^-$ from this work with the measurement from the ALICE collaboration [11].

This gives the opportunity to perform cross checks and use the two distributions in the future to determine systematic uncertainties. The two distribution of $C(k^*)$ are shown in Figure 15 for the k^* region near the threshold and for a larger range of k^*.

In the plots it can be seen that in the K^-_{down} sample the first bin has zero entries, this is due to no signal events occurring there. The statistics for the down sample is lower which is expected from the yield after the stripping lines, but in both samples an enhancement near the thresholds can be seen. The acceptance effects of the detector are visible but not as present as in $p - \Xi^-$. In the comparison with the ALICE data they are confirming each other. Here also the difference in the statistics is visible. The comparison is plotted in Figure 15.

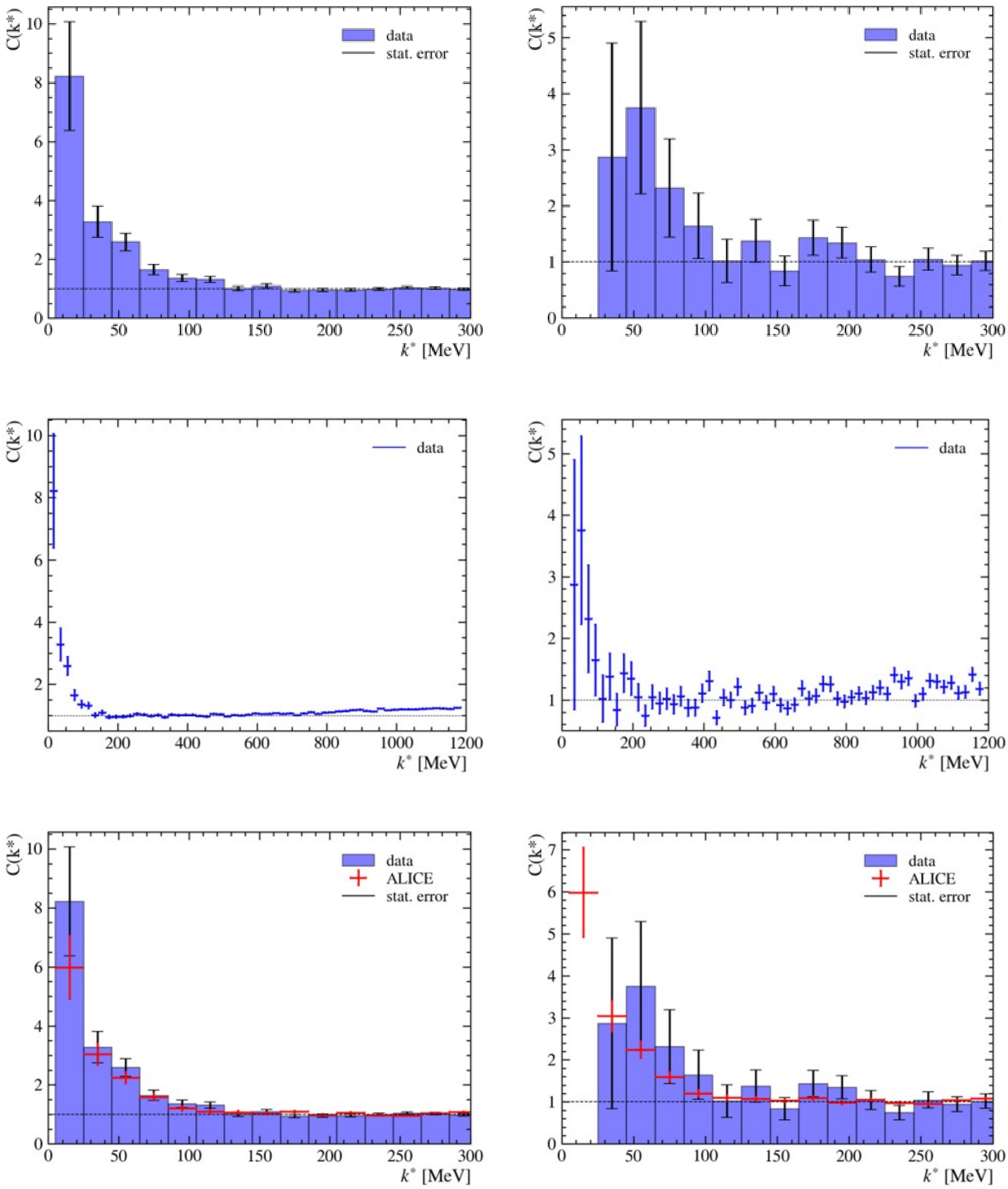

Figure 15: Correlation function of $p-\Omega^-$ for the two different stripping lines in the rage of $k^* \in [5;300]$MeV (first row), in the rage of $k^* \in [5;1205]$MeV (second row) and in the rage of $k^* \in [5;300]$MeV compared to the ALICE (red) (third row). On the left column the results for K^-_{long} and on the right for K^-_{down}. Only the statistical error is plotted for all data sets and the reference line for no interaction at 1 is given as a dotted line.

3 Run3 data

Since the Upgrade I of the LHCb detector in LS2 the detector is now equipped with a 40MHz readout system and the hardware trigger is removed and major parts of the detector were upgraded. For the femtoscopy studies dedicated HLT2 trigger lines are in place but were not tested on real data before. The aim of this study is to verify that these trigger lines work on Run3 2024 data and get a first estimate of the yield of the different trigger lines. All correlation systems which have dedicated trigger lines are listed in Table 6. The first systems till the $\Omega^- - \Omega^-$ use HLT1SMOG2 lines for the creation of Λ^0 particles. The second batch of correlation systems uses HLT1 information from the NoBias stream from pp-collisions.

In the study only one .DST file with the MagnetUp 2024 configuration is used as an input in a local DaVinci job. The condition is chosen such that the recorded data was collected after the technical stop (TS) in July. In the .DST file a total number of 49.904 events are saved and it is from the sprucing 2024c2 line. The focus lies on lines like $p - \Omega^-$ and $p - \Xi^-$ as well as on new charm baryon lines. It is proven that the trigger lines work and produce the expected mass peaks. The mass peaks for selected trigger lines after the processing and no additional cuts can be seen in Figure 16.

The plots show the mass peaks very clearly. One can see that in contrary to the initial Run2 data the background for Ω^- and Ξ^- is reduced and the yield for the $p - \Omega^-$ line is already to this date larger than the total Run2 data. After the TS from 19.07 to 16.08, 26.514 MagnetUp .DST files after sprucing are already available on DIRAC. The yield per .DST file can be read of the plot in Figure 16 which will lead to approximately 80M candidates for the $p - \Omega^-$ with already tighter selection requirements than in Run2. The yield of the total Run2 data was 26.514*3159 $\approx$ 84 million events. This increased statistics will be reduced by offline selection cuts, but since they are studied this is a straight forward task. One has to keep in mind that the more interesting number is the yield after the selection below a k^* of 100 MeV. In Run2 for $p - \Xi^-$ that is around 400 and now already 68 after one .DST file and already reduced background, but the total amount is not so promising, since the yield $843 * 26.514 = 22$M is only around a third of the yield in 2018.

These results show the capability of the new HLT2 trigger line but for some lines the offline selection cuts need to be determined.

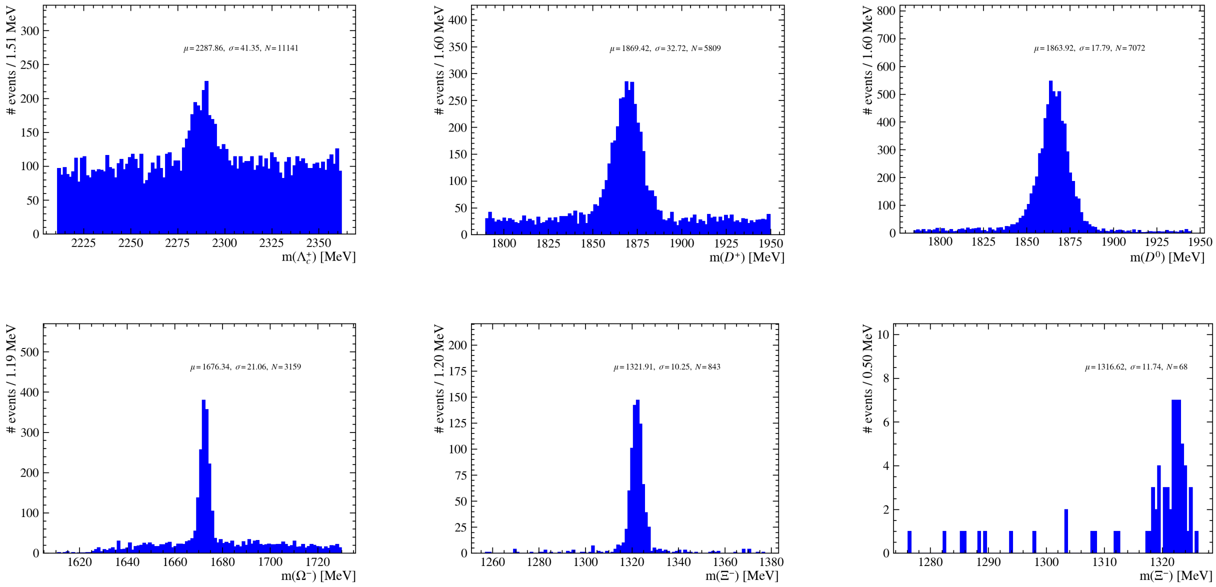

Figure 16: Mass peaks of selected HLT2 trigger lines of p-X after DaVinci without additional selections. Mass distribution of Λ_c on the top left, $m(D^+)$ on the top middle, $m(D^0)$ on top left, $m(\Omega^-)$ on second row left, $m(\Xi^-)$ in the middle of the second row and $m(\Xi^-)$ only for a k^* region up to 100 MeV in the second row on the right. The mean and the standard deviation of the histograms are give in the plots with the assumption that they follow a Gaussian distribution and in addition the yield of the sample is given.

Table 6: Summary of the HLT2 lines for femtoscopy in Run3.

Correlation system	**HLT2 line: Hlt2IFTTurbo Femtoscopy**	**prescaling**
$\Lambda^0 - p$	LambdaP	1e-3
$\Lambda^0 - \Lambda^0$	LambdaLambda	0.1
$\Xi^- - p$	XiP	0.1
$\Xi^- - \Lambda^0$	XiLambda	1
$\Xi^- - \Xi^-$	XiXi	1
$\Omega^- - p$	OmegaP	1
$\Omega^- - \Lambda^0$	OmegaLambda	1
$\Omega^- - \Xi^-$	OmegaXi	1
$\Omega^- - \Omega^-$	OmegaOmega	1
$\Lambda_c^+ - p$	LcP	1
$\Lambda_c^+ - \Lambda^0$	LcLambda	1
$\Xi^- - \Lambda_c^+$	LcXi	1
$\Omega^- - \Lambda_c^+$	LcOmega	1
$\Xi_c^+ - p$	XicpP	1
$\Xi_c^+ - \Lambda^0$	XicpLambda	1
$\Xi_c^+ - \Xi^-$	XicpXi	1
$\Xi_c^0 - p$	XiczP	1
$\Xi_c^0 - \Lambda^0$	XiczLambda	1
$\Xi_c^0 - \Xi^-$	XiczXi	1
$D^0 - p$	DzP	0.1
$D^0 - \Lambda^0$	DzLambda	1
$D^0 - \Xi^-$	DzXi	1
$D^0 - \Omega^-$	DzOmega	1
$D^+ - p$	DpP	0.1
$D^+ - \Lambda^0$	DpLambda	1
$D^+ - \Xi^-$	DpXi	1
$D^+ - \Omega^-$	DpOmega	1

4 Conclusion

This work presents the first measurement of a correlation function between a nucleon and a hyperon at the LHCb experiment. It is probed via the two-particle final state correlation function using the fraction of the number of same and number of mixed events. The results are shown in k^* bins of 20 MeV to be consistent with the measurement from ALICE.

The interactions between $p-\Xi^-$ and $p-\Omega^-$ are classified as attractive which confirms a measurement of the ALICE collaboration from 2020. The measurement is based on a precise selection of the involved particles. The selection for the hyperons is based on a FoM and enhances the purity of the sample to $> 99\%$ for Ω^-_{down} and Ξ^- and $> 95\%$ for Ω^-_{long}. A key challenge presented in this work is the selection of the p_{bach} from $K^{\pm}$ and $\pi^{\pm}$.

This work marks the first step towards a larger investigation of measuring correlation functions at LHCb with future Run3 data. Run3 data will lead to a higher statistics and the investigation of not yet measured interactions via the two-particle correlation.

A first look at new Run3 data for the implemented HLT2 femtoscopy lines shows that the output of the lines looking at the mass spectra of the hyperons give reasonable mass peaks around the PDG values. The yield for $p-\Omega^-$ from 19.07 to 16.08 , corresponding to 2.4 fb^{-1}, is estimated to supersede the total Run2 yield with 84 million events after the sprucing and no additional offline selection cuts. This is a promising start of the Run3 femtoscopy analysis.

Acknowledgement

I want to express my deepest gratitude to Prof. Mikhail Mikhasenko and Dr. Thomas Pöschl for providing me the opportunity to work on this project and participate in the summer student program. They introduced me to this nice field of research which I would have not encountered and supported me always through the summer.

I want to thank my office mates, which were, are and hopefully will be a positive enhancement to my life. The summer would have been less glorious without you two. Thank you Chinese grandpa and Sumpfmonster. I want to thank also the friendly neighbour next door which did not disturb us since he was not present so often.

I want to thank also the Michigang for the broken stove after the hot pot and to the one whom we converted to his true purpose. Special thanks also to all the people I have met during my stay at CERN and made it an unforgettable summer. I want to thank the LHCb group here at CERN for the warm welcome and the support during my stay and the Heidelberg LHCb group for there passion to let us be a shadow of the control room.

At the end I want to thank my family and friends which supported me all the time.

References

1. Vidaña, I. Hyperons: the strange ingredients of the nuclear equation of state. *Proceedings of the Royal Society A: Mathematical, Physical and Engineering Sciences* **474,** 20180145. eprint: https://royalsocietypublishing.org/doi/pdf/10.1098/rspa.2018.0145. https://royalsocietypublishing.org/doi/abs/10.1098/rspa.2018.0145 (2018).
2. Haidenbauer, J., Meißner, U.-G. & Nogga, A. Hyperon–nucleon interaction within chiral effective field theory revisited. *The European Physical Journal A* **56.** ISSN: 1434-601X. http://dx.doi.org/10.1140/epja/s10050-020-00100-4 (Mar. 2020).
3. Iritani, T. & for HAL QCD Collaboration. *HAL QCD method and Nucleon-Omega interaction with physical quark masses* 2018. arXiv: 1811.06232 [hep-lat]. https://arxiv.org/abs/1811.06232.
4. ALICE Collaboration. Unveiling the strong interaction among hadrons at the LHC. *Nature* **588,** 232–238. ISSN: 1476-4687. http://dx.doi.org/10.1038/s41586-020-3001-6 (Dec. 2020).
5. Mihaylov, D. L. *et al.* A femtoscopic correlation analysis tool using the Schrödinger equation (CATS). *The European Physical Journal C* **78.** ISSN: 1434-6052. http://dx.doi.org/10.1140/epjc/s10052-018-5859-0 (May 2018).
6. Hohlweger, B. *First observation of the* $p-\Xi^-$ *interaction via two-particle correlations* PhD thesis (Technical University of Munich, Munich, 2020).
7. Vidana, I., Feijoo, A., Albaladejo, M., Nieves, J. & Oset, E. *Femtoscopic correlation function for the* $T_{cc}(3875)^+$ *state* 2023. arXiv: 2303.06079 [hep-ph]. https://arxiv.org/abs/2303.06079.
8. Johnson, N. L. Systems of Frequency Curves Generated by Methods of Translation. *Biometrika* **36,** 149–176. ISSN: 00063444, 14643510. http://www.jstor.org/stable/2332539 (2024) (1949).
9. LHCb detector performance. *International Journal of Modern Physics A* **30,** 1530022. ISSN: 1793-656X. http://dx.doi.org/10.1142/S0217751X15300227 (Mar. 2015).
10. Mariani, S. *Fixed-target physics with the LHCb experiment at CERN* PhD thesis (Universita e INFN, Firenze (IT)/CERN, 2022).

11. ALICE Collaboration. *"Table 1" of "A new laboratory to study hadron-hadron interactions" (Version 2)* HEPData (dataset). https://doi.org/10.17182/hepdata.100195.v2/t1. 2022.